machines

MDPI

Article

The Grid-Forming Operation of a Modified Delta-Connected Cascaded H-Bridge Multilevel Inverter with PV Integration

Abdullah M. Noman

Electrical Engineering Department, College of Engineering, Prince Sattam Bin Abdulaziz University, Al-Kharj 11942, Saudi Arabia; a.noman@psau.edu.sa

Abstract

The increasing penetration of inverter-based renewable energy resources, especially photovoltaic (PV) systems, has decreased the available system inertia and introduced challenges in maintaining stable grid-forming operation. This paper presents a grid-forming photovoltaic multilevel inverter (MLI) with a modified delta-connected cascaded H-bridge (CHB) multilevel configuration. The proposed system decreases the number of semiconductor switches and provides inherent voltage balancing, while also achieving high power quality, rendering it suitable for grid-forming applications. Each H-bridge cell is connected to an isolated Cúk converter to enable maximum power point tracking (MPPT) of distributed PV modules, allowing for flexible and modular DC-side integration. The proposed MLI operates as a virtual synchronous generator. A control scheme is proposed to attain grid-forming capability, hence providing stable voltage and frequency support. Moreover, a DC-link voltage regulation strategy is also developed to maintain the DC-link voltage at the reference voltage. A detailed mathematical model is developed to characterize the associated dynamics of the proposed MLI and the control system with a grid interface. The model is built in the SIMULINK environment, and the simulation results are presented under variations in solar radiation and grid voltage disturbances to exhibit the functionality of the proposed system and the effectiveness of the control scheme in providing a well-damped frequency response and stable generated voltage and currents. The results demonstrate stable frequency regulation with a settling time of approximately 0.3 s, and the output current exhibits low harmonic distortion, with a Total Harmonic Distortion (THD) of about 0.53%. Simulation results show stable operation and confirm that the proposed approach is a competitive solution for PV-based grid-forming applications.

Keywords: grid-forming inverter; modified delta-connected cascaded H-bridge inverter; multilevel inverter; photovoltaic systems; virtual synchronous generator; grid-connected converters

Check for updates

Academic Editor: Mohamed Abdelrahem

Received: 7 April 2026
Revised: 15 May 2026
Accepted: 20 May 2026
Published: 25 May 2026

Copyright: © 2026 by the author. Licensee MDPI, Basel, Switzerland. This article is an open access article distributed under the terms and conditions of the Creative Commons Attribution (CC BY) license.

1. Introduction

The rapid penetration of inverter-based renewable energy resources (RESs), especially PV systems, has significantly reduced the simultaneous inertia available in modern energy systems, raising severe challenges in stability in both transmission and distribution networks. Conventional grids depend on synchronous machines that inherently offer inertia, fault current, and grid-forming functionality. As inverter-based resources replace this machinery, the grid increasingly relies on converters that are inherently grid-following and demonstrate low inertial response [1]. This structural change has prompted substantial investigation into grid-forming inverters (GFIs), including virtual synchronous generators

(VSGs), which permit power-electronic converters to actively regulate grid voltage and frequency instead of passively following them. GFIs are now considered a crucial enabling technology for ensuring stability in weak and low-inertia power systems characterized by strong renewable energy integration [2]. The VSG concept has emerged as a leading grid-forming method due to its strong physical similarity to synchronous machines and its conformity with established power system theory [3,4]. Preliminary foundational research has established that the electromechanical swing dynamics of synchronous generators could be digitally emulated within inverter control loops, facilitating decentralized frequency and voltage regulation independent of substantial rotating masses [4,5]. These investigations have shown that integrating swing-equation-based dynamics into inverter controls can offer artificial inertia and droop features, thus enhancing transient frequency response and enabling power sharing across distributed generators.

While the VSG concept primarily focuses on control design, the overall performance of grid-forming inverters is not determined by control alone but is also strongly influenced by the underlying inverter topology. The selection of inverter topology is equally vital in influencing system performance, efficiency, and scalability. Traditional two-level voltage source inverters are common in grid-connected applications because of their simplicity; yet, they suffer notable switching losses, reduced voltage levels, and higher harmonic distortion, especially in medium- and high-power systems [6].

To reduce these drawbacks, multilevel inverter (MLI) topologies have been widely investigated for VSG operation. Their suitability for grid-forming operation is strongly affected by the number of semiconductor switches, DC sources, passive components, voltage stress, and voltage-balancing requirements [7–9]. These factors become more important in medium- and high-power grid-forming systems, where the inverter operates as a voltage source and is required to generate high-quality voltage with stable dynamic behavior. Classical MLI topologies, such as CHB, NPC, and FC, still face practical challenges, including increased switch count, complex control, capacitor voltage balancing, and higher total standing voltage when the number of voltage levels increases [10,11]. Therefore, reduced-component and structurally improved MLI topologies remain an important direction in power converter design [12].

Despite these benefits, traditional CHB configurations—particularly delta-connected topologies—face various practical difficulties, such as circulating currents between phases and a greater number of switches [13]. These constraints can adversely affect system efficiency and dynamic performance, especially in grid-forming operations when voltage quality and stability are essential. Consequently, the development of modified multilevel inverter topologies that diminish hardware complexity while preserving the advantages of CHB architectures has emerged as an important study focus.

Recent studies have emphasized that DC-link voltage regulation is important in grid-forming PV converters, especially when the DC source cannot be treated as a stiff source. Therefore, the PV source dynamics and limitations should be considered in the control design to maintain DC-link stability [14]. This issue becomes more critical in PV-fed grid-forming systems due to the variability in solar power and the interaction between the DC-side and AC-side dynamics. Accordingly, several recent studies have investigated the interaction between PV-side dynamics and grid-forming operation. In addition to converter topology considerations, several recent studies have investigated the interaction between PV-side dynamics and grid-forming operation. In [7], a CHB-based PV converter using VSG control was proposed to support grid operation through modular active power reserve by selecting reserved cells to provide the power buffer between the VSG and PV power for grid frequency support. Coordinated DC/DC and DC/AC grid-forming control strategies for PV-connected systems were also investigated in [15], where the effect of DC-

link voltage variations caused by direct PV connections was considered in a PV plus battery energy storage configuration. Moreover, MMC-based grid-forming implementations have been studied for medium- and high-power applications [16]. Although these studies demonstrated the importance of DC-link dynamics and frequency-support capability in grid-forming converters, they were mainly focused on conventional converter structures or battery-supported implementations rather than PV-fed multilevel inverter systems with coordinated DC-link and frequency interaction.

From another point of view, previous studies have indicated that VSG implementations with static inertia and damping parameters are inadequate under fluctuating operating conditions. Static parameter selection presents a critical trade-off: high inertia values can significantly diminish the Rate of Change of Frequency but frequently result in a sluggish system response and heightened oscillatory behavior, whereas low inertia values enhance responsiveness at the expense of frequency support and damping [3,17]. This constraint has prompted extensive research into adaptive and optimization-driven VSG control techniques. Heuristic, model-free methodologies, such as fuzzy logic controllers and coordinated adaptive strategies, have been suggested to dynamically modify inertia and damping parameters in accordance with varying system conditions [18,19]. Recent studies have introduced predictive and optimization-based VSG frameworks. Model predictive control (MPC)-inspired and adaptive predictive VSG (AP-VSG) techniques clearly address multi-objective performance requirements [20–22]. These techniques provide enhanced performance and a more systematic tuning procedure; however, their computational complexity and dependence on precise system models pose challenges for real-time implementation and stability amid parameter uncertainty.

Voltage imbalance constitutes a notable practical difficulty for VSG-controlled inverters, especially in distribution networks with single-phase loads and asymmetrical operating conditions. Unbalanced voltages generate negative-sequence currents and double-frequency (2ω) power oscillations, which can destabilize VSG-controlled converters if not adequately addressed. To resolve this issue, numerous studies have enhanced VSG control architectures by using negative-sequence extraction, balanced output current techniques, and selected compensation techniques, including constant active power (CAP) and constant reactive power (CRP) operation [18,23].

Adaptive inertial and damping control laws have also been proposed in the literature to improve the transient response and frequency stability of VSG-based converters under varying operating conditions [23]. In [23], an adaptive VSG control strategy based on a conventional two-level inverter with a DC source was developed to enhance frequency regulation under unbalanced grid-voltage conditions through adaptive adjustment of the inertia and damping coefficients. This study demonstrated the importance of coordinated inertia and damping selection for improving dynamic performance and stability. However, the work was mainly focused on conventional inverter structures rather than PV-fed multilevel grid-forming systems.

Grid strength and network impedance characteristics also play a critical role in VSG performance. In weak grids, the coupling between active and reactive power and voltage angle and magnitude becomes more pronounced, increasing sensitivity to controller parameter selection and potentially exciting poorly damped oscillatory modes. To improve robustness, several studies have proposed adaptive VSG strategies that incorporate online estimation of grid impedance, short-circuit ratio, or Thevenin equivalents, enabling network-aware tuning of inertia, damping, and virtual impedance parameters [20]. While effective in principle, these approaches depend on reliable real-time estimation and appropriate bandwidth separation to avoid adverse interactions.

From an implementation perspective, computational burden and real-time feasibility remain important considerations. Although evolutionary optimization techniques and MPC-based controllers can deliver superior dynamic performance, their iterative nature may exceed the computational capabilities of embedded control platforms. Consequently, many practical solutions adopt hybrid approaches that combine offline optimization with simplified online adaptive laws or supervisory switching mechanisms [19,24]. Recent work has also explored low-order observers and event-triggered adaptation schemes to reduce computational requirements while maintaining acceptable performance [25,26].

Validation methodologies have evolved alongside control strategies. In addition to extensive MATLAB/Simulink studies, hardware-in-the-loop (HIL) testing and microgrid-scale experimental platforms are increasingly employed to evaluate adaptive VSG performance under realistic operating conditions, including measurement noise, communication delays, and component non-idealities [23,27,28].

The implementation of VSG concepts in PV systems introduces additional practical challenges. Unlike synchronous machines, PV systems do not possess intrinsic energy storage, causing the DC-link voltage to be strongly influenced by solar irradiance variations, MPPT operation, and AC-side power exchange. Therefore, assuming stiff or constant DC sources may simplify the analysis, but it does not fully represent the dynamic behavior of practical PV-fed grid-forming systems. In addition, most existing studies mainly focus on the control strategy while treating the inverter topology and DC-link regulation separately. However, the inverter topology, DC-link dynamics, and grid-forming control jointly affect voltage quality, dynamic performance, and system stability, particularly under varying operating conditions and grid disturbances.

Table 1 compares representative grid-forming converter studies from the literature in terms of converter topology, DC-side implementation, DC-link/frequency coordination approach, VSG dynamic parameter consideration, and representative evaluation conditions. The comparison highlights different system-level implementation perspectives adopted for grid-forming operation, including the coordinated integration framework considered in the proposed work.

Table 1. A comparison of representative grid-forming converter studies and the proposed system.

Ref.	Converter Structure	DC-Side Representation	DC-Link/Frequency Coordination Approach	VSG Dynamic Parameter Consideration	Main Implementation Focus	Representative Evaluation Conditions
[7]	Conventional CHB PV converter	PV-fed modular DC-link	Power-reserve-based frequency support within VSG operation	Frequency-support operation through VSG control	Control strategy for CHB converter with combination of MPPT and VSG	PV power reserve operation
[15]	Series-connected PV converters	PV-fed converter system	Coordinated DC/DC and DC/AC converter regulation	Dynamic coordination between DC/DC and DC/AC stages	Control design for modular PV-powered GFM converters	PV power and frequency disturbances
[16]	MMC	DC-source-fed MMC structure	MMC internal energy/frequency coordination	Investigated for MMC-VSG weak-grid operation	MMC-based VSG implementation for weak grids	Weak-grid MMC operation

Table 1. *Cont.*

Ref.	Converter Structure	DC-Side Representation	DC-Link/Frequency Coordination Approach	VSG Dynamic Parameter Consideration	Main Implementation Focus	Representative Evaluation Conditions
[23]	Two-level VSI	Simplified DC-source representation	Adaptive inertia and damping regulation	Adaptive inertia and damping tuning	Adaptive VSG control under imbalanced conditions	Grid-voltage imbalance
[29]	Two-level inverter with PV+BESS DC coupling	PV and battery-supported DC-link	Battery-assisted DC-link support	Grid-forming operation with battery-supported DC-link	Integrated PV+BESS grid-forming operation	Grid disturbance conditions
[30]	Modified delta-connected CHB MLI	Basic DC-side/topology validation	Topology-oriented validation without VSG dynamic analysis	Dynamic parameter analysis not within study scope	Validation of modified delta-connected CHB topology	Topology verification
Proposed work	Modified delta-connected CHB MLI	Supervisory-regulated PV-fed DC-link implementation	Supervisory DC-link/frequency coordination within VSG dynamics	Inertia and damping influence evaluated together with DC-link supervisory interaction	Coordinated PV-fed grid-forming operation using modified delta-connected CHB MLI with reduced switch count and DC-link supervisory interaction	Irradiance variation, grid-voltage disturbance, and parameter variation

Based on the previous discussion and the comparison presented in Table 1, the present work investigates a PV-fed grid-forming system based on a modified delta-connected CHB MLI and a VSG-based control framework. The adopted topology builds upon the configuration presented in [30] and extends its application to PV-based grid-forming operation. Compared with conventional delta-connected CHB structures, the proposed topology generates the same voltage levels with a lower number of power switches, while maintaining modularity, inherent voltage balancing capability, and elimination of circulating currents without requiring additional inductive components or grid-side transformers. In addition to the converter topology, the proposed work incorporates a supervisory signal derived from the DC-link controller into the frequency-forming loop, enabling coupling between PV-fed DC-link dynamics and the AC-side frequency response. The proposed control structure also integrates inertia- and damping-dependent dynamics within the DC-link regulation loop to coordinate DC-side voltage regulation with the VSG frequency dynamics and evaluate their influence on the system dynamic behavior.

The proposed system is further evaluated under solar irradiance variation, grid-voltage disturbances, and different inertia and damping conditions to examine the coordinated interaction between DC-link dynamics and grid-forming operation under varying PV operating conditions. Therefore, the proposed work provides a coordinated implementation framework for grid-forming operation of a modified delta-connected CHB multilevel

inverter with supervisory DC-link/frequency interaction. The remainder of this paper is organized as follows. Section 2 presents the proposed VSG system. Section 3 describes the mathematical modeling and the proposed control scheme. Simulation results are presented in Section 4, while Section 5 concludes this paper.

2. System Configuration of the Proposed Grid-Forming MLI-Based PV

2.1. Description of the Proposed Grid-Forming MLI

The proposed grid-forming system is based on the three-phase modified delta-connected cascaded H-bridge (CHB) multilevel inverter that generates a nine-level line-to-line output voltage. The system is built around a modified delta-connected cascaded H-bridge (CHB) multilevel inverter that addresses several limitations of conventional two-level, star-connected CHB, and classical delta-connected CHB topologies when used in grid-forming applications.

To the best of the author's knowledge, this configuration has not been previously implemented in grid-forming VSG-based operation. In this work, the topology is further adapted and integrated within a grid-forming PV system. The proposed system is shown in Figure 1. Compared with the conventional delta-connected CHB, the modified configuration is able to achieve higher line-to-line voltage levels while using fewer semiconductor switches and DC sources, with reduced voltage stress on the power devices. It also suppresses circulating currents inherently and maintains voltage self-balancing without the need for additional inductive components or grid-side transformers. These features result in a simpler structure, improved efficiency, and better overall performance. For clarity, a simple comparison between the conventional delta-connected CHB and the adopted topology is summarized in Table 2. These structural advantages make this topology particularly suitable for grid-forming operation, where the inverter is required to produce high-quality voltage with reduced filter sizes and maintain stable dynamic behavior.

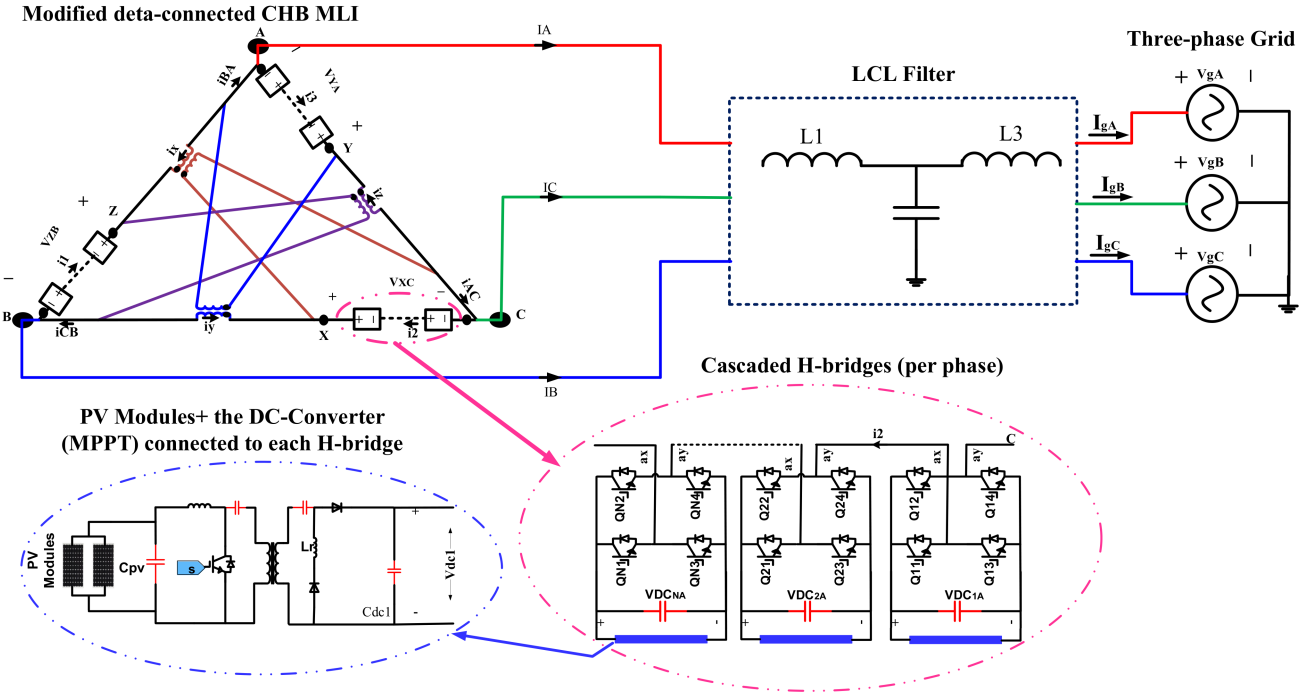


Figure 1. The proposed VSG-based modified delta-connected CHB MLI topology.

Table 2. A quantitative comparison between the conventional delta-connected CHB and the modified topology (for the same output voltage level).

Feature	Conventional Delta-Connected CHB	Modified Delta-Connected CHB
Number of H-bridge cells	12	6
Number of switches	48	24
Number of DC sources	12	6
DC-link capacitors	12	6
Additional inductors	3	Not required
Intermediate transformers	Not used	3
Grid-side transformer requirement	May be required	Not required if voltage amplification is provided by intermediate transformers

The comparison is based on an equivalent output voltage level configuration, as reported in [30].

In the present work, this modified delta-connected CHB MLI serves as the grid-forming voltage source and is combined with a synchronous virtual machine-based control strategy to establish voltage and frequency without reliance on phase-locked loops.

Each H-bridge cell is supplied through an isolated Ćuk DC–DC converter connected to an individual PV array. The use of isolated Ćuk converters enables independent MPPT, provides galvanic isolation, and offers continuous input current characteristics that are well-suited for PV systems. In addition, the DC–DC conversion stage effectively decouples PV-side dynamics from the AC grid, allowing stable grid-forming operation under variable solar irradiance. Regulated DC-link voltage controllers ensure stable energy buffering and controlled interaction between PV power availability and grid-forming behavior.

By integrating an advanced multilevel inverter topology with isolated DC–DC interfacing, realistic PV modeling, and synchronous virtual machine-based grid-forming control, the proposed system provides a comprehensive framework for analyzing PV-fed grid-forming operation under varying operating conditions.

The line-to-line voltage levels from the proposed modified delta-connected CHB MLI are given as:

$$\begin{aligned} v_{AB} &= \tfrac{N_1}{N_2} v_{CX} + v_{ZB}, \\ v_{BC} &= \tfrac{N_1}{N_2} v_{AY} + v_{XC}, \\ v_{CA} &= \tfrac{N_1}{N_2} v_{BZ} + v_{YA}, \end{aligned} \tag{1}$$

where v_{ZB}, v_{XC}, and v_{YA} are voltages of the CHB cells of phases A, B, and C, respectively, and $\frac{N_1}{N_2}$ is the coupled transformers' turn ratios.

The root-mean square (RMS) values of the voltages across each CHB arm in the proposed topology can be given as:

$$\begin{aligned} V_{ZB} &= \tfrac{N m_a V_{dc}}{\sqrt{2}} \angle 0^o, \\ V_{XC} &= \tfrac{N m_a V_{dc}}{\sqrt{2}} \angle -120^o, \\ V_{YA} &= \tfrac{N m_a V_{dc}}{\sqrt{2}} \angle +120^o, \end{aligned} \tag{2}$$

On the other hand, the output terminal currents of the modified delta-connected CHB MLI can be given as

$$\begin{bmatrix} i_A \\ i_B \\ i_C \end{bmatrix} = \begin{bmatrix} -i_3 - i_x + \frac{N_1}{N_2} i_y \\ -i_1 - i_y + \frac{N_1}{N_2} i_z \\ -i_2 - i_z + \frac{N_1}{N_2} i_x \end{bmatrix}, \tag{3}$$

where i_A, i_B, and i_C are the line currents of phases A, B, and C, respectively, i_x, i_y, and i_z are the currents in the primary side of the coupled transformers T_x, T_y and T_z, respectively, and i_1, i_2, and i_3 are the currents flowing inside the CHB cells of the phases AB, BC, and CA, respectively.

2.2. Loss Considerations

Loss and efficiency analyses are presented to further support the performance of the modified delta-connected CHB MLI topology. The total power losses of the inverter can be expressed as:

$$P_{\text{loss}} = P_{\text{cond}} + P_{\text{sw}} + P_{\text{tr}}, \tag{4}$$

where P_{cond}, P_{sw}, and P_{tr} represent the semiconductor conduction losses, switching losses, and transformer-related losses, respectively.

The conduction losses of the semiconductor devices can be approximated as:

$$P_{\text{cond}} = \sum_{i=1}^{N_s} \left(V_{\text{on},i} I_i + R_{\text{on},i} I_i^2 \right), \tag{5}$$

where N_s is the number of conducting switches, $V_{\text{on},i}$ and $R_{\text{on},i}$ are the on-state voltage drop and resistance, and I_i is the current through each switch.

The switching losses are given by:

$$P_{\text{sw}} = \sum_{i=1}^{N_s} f_s (E_{\text{on},i} + E_{\text{off},i}), \tag{6}$$

where f_s is the switching frequency, and $E_{\text{on},i}$ and $E_{\text{off},i}$ are the switching energies of each device.

The overall efficiency of the inverter can be defined as:

$$\eta = \frac{P_{\text{out}}}{P_{\text{out}} + P_{\text{loss}}}, \tag{7}$$

From the above expressions, it can be observed that both conduction and switching losses are directly proportional to the number of semiconductor switches. Therefore, the reduced switch count in the proposed modified delta-connected CHB topology leads to lower total losses compared to conventional CHB configurations.

A more detailed loss analysis of the modified delta-connected CHB MLI topology can be found in [30].

3. Mathematical Modeling of the Proposed Grid-Forming MLI PV System

The electrical relationships provided in Section 2, including the line voltage and current expressions, form the basis for modeling the behavior of the presented MLI. These equations describe how the converter interacts with the AC side and define the power exchange with the grid. This part focuses on the dynamic model of the system, including the DC-link voltage dynamics and the VSG-based control structure to explain the relationship between the DC-side energy source and the AC-side grid-forming operation. This section explores the mathematical modeling of the proposed grid-forming photovoltaic inverter system. The formulation encapsulates the dynamic interaction of the VSG control, the voltage-forming loops, the LCL filter interface, and the DC-link voltage regulation related to the PV sources. The overall control structure of the proposed system is illustrated in Figure 2, which serves as the basis for subsequent modeling development. The model

is derived directly from this control architecture and does not rely on stiff DC-source assumptions, thereby enabling a realistic representation of PV-fed grid-forming operation under variable irradiance conditions.

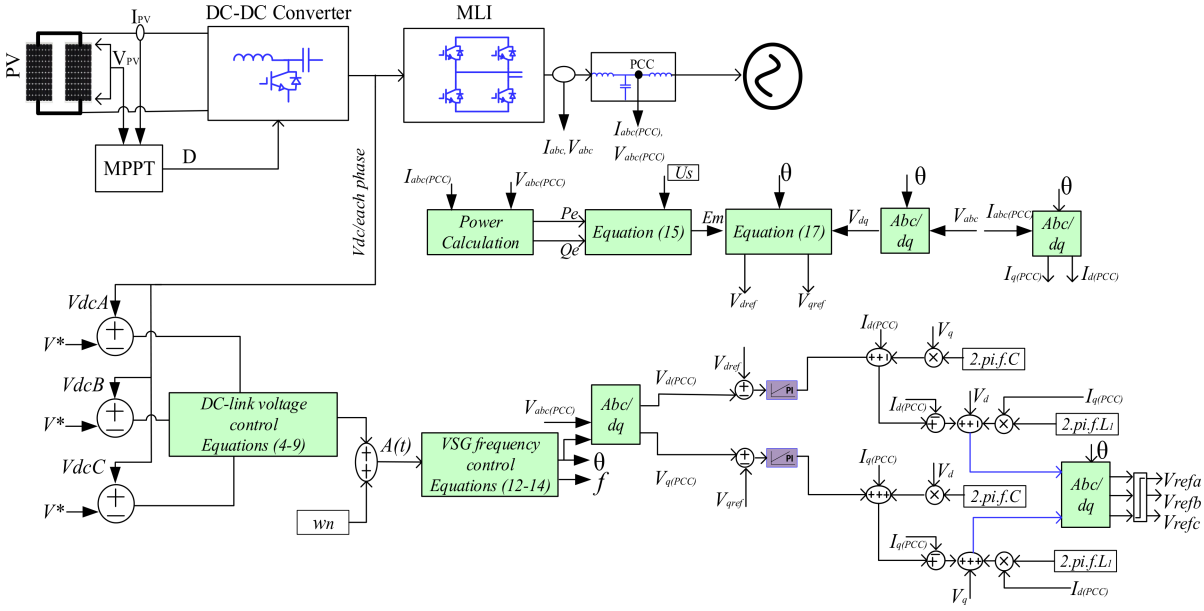


Figure 2. The proposed control scheme.

The proposed grid-forming MLI system is supplied by PV sources through isolated DC–DC Cúk converters, which are connected to the cascaded H-bridge cells through the DC-link capacitors. The DC-link dynamics play an important role in shaping the interaction between PV energy availability and grid-forming operation, making their explicit representation essential.

For simplicity, each phase of the modified delta-connected cascaded H-bridge inverter consists of two series-connected H-bridge cells, resulting in six independent DC-link capacitors. For each H-bridge cell k, the DC-link voltage dynamics are governed by the capacitor power balance equation:

$$C_{dc,k}\frac{dV_{dc,k}}{dt} = I_{\text{Cúk},k} - I_{HB,k}, \tag{8}$$

where $V_{dc,k}$ is the DC-link voltage of the k-th H-bridge, $C_{dc,k}$ is the corresponding DC-link capacitance, $I_{\text{Cúk},k}$ is the output current of the associated isolated Cúk converter operating under MPPT, and $I_{\text{HB},k}$ is the current drawn by the inverter cell.

The current relationship given in (3) defines the inverter output currents, and, therefore, the power exchanged with the grid. Since the DC-link voltage depends on the balance between the input PV power and the output AC power, this relationship plays an important role in the DC-link voltage dynamics and the overall control design.

For control purposes, the phase DC-link voltage of each phase is defined as:

$$V_{dc,x} = \frac{V_{dc1x} + V_{dc2x}}{2}, x \in \{a, b, c\}, \tag{9}$$

where V_{dc1x} and V_{dc2x} are the measured DC-link voltages of the two cascaded H-bridge cells in phase x. The corresponding DC-link voltage error signal is:

$$e_{dc,x} = V^{\star}_{dc,x} - V_{dc,x}. \tag{10}$$

where $V_{dc,x}$ is the average DC-link voltage of phase x, and $V^{\star}_{dc,x}$ is the DC-link voltage reference.

To regulate the DC-link voltage under irradiance variations and power imbalance conditions, the error signal is processed by using a lead–lag compensator implemented in transfer-function form as

$$C_{dc}(s) = K_{dc}\frac{s + K_1}{Js + K_2 D}, \tag{11}$$

where K_{dc} is the compensator gain, and the parameters J and D are the virtual inertia and damping used in the VSG frequency dynamics.

This formulation intentionally aligns the dominant DC-link control dynamics with the time constants of the virtual electromechanical system, thereby facilitating coordinated energy and frequency regulation. The compensator output for each phase is:

$$A_x = C_{dc}(s).\, e_{dc,x} \tag{12}$$

where A_x is the phase-wise DC supervisory signal after compensation. The three phase-wise compensator outputs are then aggregated to form a global DC supervisory signal (A) :

$$A(t) = (A_a(t) + A_b(t) + A_c(t)) \tag{13}$$

where $A(t)$ is the aggregated DC supervisory signal obtained from the DC-link voltage controllers. This supervisory signal is incorporated into the frequency-forming control loop, allowing DC-link voltage regulation to be achieved through smooth adaptation of the grid-forming dynamics. This DC-link modeling framework ensures that variations in PV power and DC-side energy availability are explicitly reflected in the control structure, enabling the stable operation of the GFI. This modeling approach also enables a direct link between DC-side energy variations and AC-side frequency dynamics, which is essential for realistic grid-forming PV operation.

From another point of view, the proposed inverter operates without a phase-locked loop. Instead, all control variables are expressed in a synchronous reference frame defined by the internally generated virtual rotor angle θ. The three-phase voltages and currents measured at the point of common coupling (PCC) are transformed into the dq reference frame using this virtual rotor angle.

The active and reactive powers injected by the inverter are measured at PCC, and they are given as:

$$P_{PCC}(t) = \frac{3}{2}(v_d i_d + v_q i_q),\ Q_{PCC}(t) = \frac{3}{2}(v_q i_d - v_d i_q), \tag{14}$$

where v_d and v_q denote the direct- and quadrature-axis PCC voltages, and i_d and i_q are the corresponding current components. These power quantities form the feedback signals for the grid-forming active and reactive power control loops.

Following the DC-link voltage regulation stage, the grid-forming behavior of the proposed inverter is realized through a VSG-based frequency control. Unlike conventional VSG implementations that assume a fixed nominal frequency and a stiff DC source, the proposed formulation explicitly incorporates the DC-link supervisory signal derived in the previous subsection, thereby coordinating AC-side frequency formation with DC-side energy availability.

The effective nominal angular frequency of the virtual machine is defined as

$$\omega_0(t) = \omega_n + A(t), \tag{15}$$

where ω_n is the rated angular frequency.

The frequency deviation relative to the effective nominal frequency is given by

$$e_\omega(t) = \omega_0(t) - \omega(t), \tag{16}$$

and is mapped into an internal synchronizing power command through a proportional synchronizing gain,

$$P_{\text{syn}}(t) = K_s\, e_\omega(t), \tag{17}$$

where $P_{\text{syn}}(t)$ is the synchronizing-power command, and K_s is the synchronizing gain that determines the strength of the coupling between the frequency deviation and the synchronizing power.

The swing dynamics of the synchronous virtual machine are implemented in deviation form as

$$\begin{gathered} J\frac{d\Delta\omega(t)}{dt} = \frac{1}{\omega_n}\left(P_{\text{syn}}(t) - P_{\text{PCC}}(t)\right) - D\,\Delta\omega(t), \\ \omega(t) = \omega_0(t) + \Delta\omega(t), \frac{d\theta(t)}{dt} = \omega(t), \end{gathered} \tag{18}$$

where $\Delta\omega(t)$ is the internal frequency deviation state, $\theta(t)$ is the virtual rotor angle used to generate the synchronous reference frame for voltage synthesis and modulation, $\omega_0(t)$ is the effective nominal angular frequency, and P_{PCC} is the measured active power at the PCC. The parameters J and D represent the virtual inertia and damping coefficient, respectively.

By injecting the DC-link supervisory signal $A(t)$ into the nominal frequency path, the proposed control introduces an intrinsic coupling between the DC-side energy and the AC-side frequency dynamics. When the DC-link voltage decreases due to reduced solar irradiance or increased power demand, the supervisory signal modifies the effective frequency $\omega_o(t)$, which in turn influences the power angle dynamics and the synchronizing power. As a result, the active power delivered to the grid is automatically adjusted according to the available DC-side energy. This mechanism inherently limits excessive power extraction and contributes to maintaining DC-link voltage stability without requiring explicit power limiting or discrete mode-switching strategies.

On the other hand, when sufficient DC-side energy is available, the virtual machine operates under standard grid-forming conditions, preserving its inertial response and frequency damping characteristics. As a result, the proposed control retains the fundamental behavior of synchronous-machine emulation, while ensuring DC-link voltage stability in PV-fed systems. This coordinated interaction between DC-side energy regulation and AC-side frequency dynamics enhances system performance by enabling the stable operation of the proposed PV-fed grid-forming MLI under varying operating conditions.

From another point of view, reactive power control is implemented through voltage magnitude adjustment, consistent with synchronous generator behavior. The reactive-power error is processed by a proportional–integral (PI) controller to generate the internal voltage magnitude reference

$$E_m = U_s + k_{pQ}(Q^\star - Q) + k_{iQ}\int (Q^\star - Q)\, dt, \tag{19}$$

where $Q^\star$ is the reactive-power reference, U_s is the nominal voltage magnitude, and k_{pQ} and k_{iQ} are the controller gains. The voltage magnitude E_m, together with the virtual angle θ, defines the three-phase voltage reference used for grid-forming operation.

Using the virtual angle $\theta(t)$ obtained from the synchronous virtual machine frequency loop, the internal three-phase voltage vector is constructed as

$$\mathbf{e}_{abc}(t) = E_m(t)\begin{bmatrix} sin\theta(t) \\ sin\left(\theta(t) - \frac{2\pi}{3}\right) \\ sin\left(\theta(t) + \frac{2\pi}{3}\right) \end{bmatrix}, \tag{20}$$

The corresponding synchronous-frame voltage components $e_d(t)$ and $e_q(t)$ are then obtained through standard coordinate transformation using the same virtual angle $\theta(t)$.

To enhance voltage robustness and emulate the internal impedance characteristics of a synchronous generator, a virtual impedance composed of R_1 and L_1 is incorporated. Accordingly, the PCC voltage references used in the inner voltage loop are generated as

$$\begin{aligned} v_d^\star(t) &= e_d(t) - R_1\, i_{Ld}(t) + \omega(t) L_1\, i_{Lq}(t), \\ v_q^\star(t) &= e_q(t) - R_1\, i_{Lq}(t) - \omega(t) L_1\, i_{Ld}(t), \end{aligned} \tag{21}$$

where i_{Ld} and i_{Lq} are the inverter-side filter currents in the synchronous frame, R_1 is the virtual resistance, L_1 is the inverter-side filter inductance, and $\omega(t)$ is the virtual angular frequency generated by the VSG frequency dynamics.

These voltage references $v_d^\star$ and $v_q^\star$ are subsequently processed by the inner voltage controller to produce the inverter modulation signals, as will be explained below.

The inverter is connected to the grid through an LCL filter composed of an inverter-side inductance L_1, a grid-side inductance L_3, and a damping branch consisting of a resistor R_2 and a capacitor C_2. In the synchronous reference frame defined by the virtual angle θ, the dynamic behavior of the inverter-side and grid-side inductors is described by

$$\begin{aligned} L_1 \tfrac{di_{1d}}{dt} &= v_{inv,d} - v_{pcc,d} + \omega L_1 i_{1q}, \\ L_1 \tfrac{di_{1q}}{dt} &= v_{inv,q} - v_{pcc,q} - \omega L_1 i_{1d}, \end{aligned} \tag{22}$$

$$\begin{aligned} L_3 \tfrac{di_{gd}}{dt} &= v_{pcc,d} - v_{g,d} + \omega L_3 i_{gq}, \\ L_3 \tfrac{di_{gq}}{dt} &= v_{pcc,q} - v_{g,q} - \omega L_3 i_{gd}. \end{aligned} \tag{23}$$

where i_{1d} and i_{1q} are the direct- and quadrature-axis currents flowing through the inverter-side inductor L_1, while i_{gd} and i_{gq} denote the grid-side currents flowing through the inductor L_3. The quantities $v_{inv,d}$ and $v_{inv,q}$ are the inverter output voltages, $v_{pcc,d}$ and $v_{pcc,q}$ are the voltages at the point of common coupling, and $v_{g,d}$ and $v_{g,q}$ represent the grid voltages expressed in the synchronous reference frame. The angular frequency ω is provided by the synchronous virtual machine frequency loop.

The damping branch dynamics are governed by:

$$\begin{aligned} &C_2 \tfrac{dv_{C2,d}}{dt} = i_{c,d}, C_2 \tfrac{dv_{C2,q}}{dt} = i_{c,q}, \\ &v_{pcc,d} - v_{C2,d} = R_2 i_{c,d}, v_{pcc,q} - v_{C2,q} = R_2 i_{c,q}. \end{aligned} \tag{24}$$

where $v_{C2,d}$ and $v_{C2,q}$ are the capacitor voltages of the damping branch in the synchronous reference frame, while $i_{c,d}$ and $i_{c,q}$ are the corresponding capacitor currents. The resistor R_2 provides passive damping of the LCL resonance by dissipating oscillatory energy, thereby improving system stability without increasing control complexity.

The voltage-forming control loop regulates the PCC voltage components in the synchronous reference frame. The inverter voltage reference is generated as

$$v_{inv,d}^\star = k_{pv}(v_d^\star - v_{pcc,d}) + k_{iv} \int (v_d^\star - v_{pcc,d})\, dt - \omega L_1 i_{1q} + v_{pcc,d}, \tag{25}$$

$$v_{inv,q}^\star = k_{pv}(v_q^\star - v_{pcc,q}) + k_{iv} \int (v_q^\star - v_{pcc,q})\, dt + \omega L_1 i_{1d} + v_{pcc,q}, \tag{26}$$

where $v_d^\star$ and $v_q^\star$ are the voltage references generated by the outer control loops, and k_{pv} and k_{iv} are the voltage-controller gains. The cross-coupling terms compensate for the rotating reference frame dynamics, ensuring decoupled voltage regulation.

These reference voltages are then transformed into the abc frame and applied to the proposed phase-shifted PWM (PSPWM), depicted in Figure 3, to generate the required switching pulses of the proposed modified delta-connected CHB MLI.

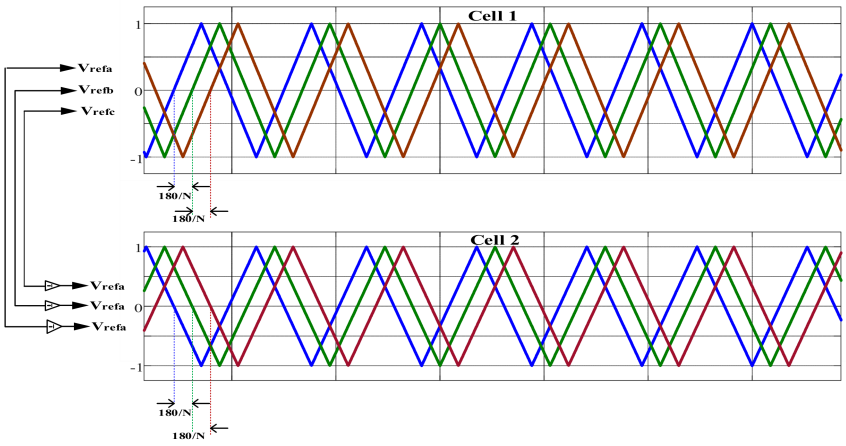


Figure 3. The PSPWM technique to drive the proposed MLI.

To provide further analytical insight into the system behavior and its stability, a simplified reduced-order small-signal analysis is derived, based on the VSG swing equation.

From (18), the frequency dynamics can be expressed as:

$$J\frac{d\Delta\omega}{dt} = \frac{1}{\omega_n}\Delta P - D\Delta\omega \tag{27}$$

where ΔP represents the small variation in active power.

Rearranging (27) yields

$$J\frac{d\Delta\omega}{dt} + D\Delta\omega = \frac{1}{\omega_n}\Delta P \tag{28}$$

Taking the Laplace transform,

$$\frac{\Delta\omega(s)}{\Delta P(s)} = \frac{1}{\omega_n(Js + D)} \tag{29}$$

This transfer function represents a stable first-order frequency dynamic for positive values of J and D. The damping coefficient D directly affects the attenuation of frequency oscillations, whereas the virtual inertia J determines the transient response speed. Therefore, the coordinated selection of J and D influences the grid-forming dynamic response under varying PV operating conditions. This analysis mainly reflects the behavior of the frequency dynamics, while the overall system performance is further verified through the simulation results under different operating conditions.

4. Simulation Results

To validate the proposed grid-forming control strategy and the modified delta-connected CHB topology, simulations were carried out in MATLAB/Simulink 2024b under various operating conditions. For simplicity purposes, only two H-bridge cells were used in each phase. The objective of the simulations is to evaluate the dynamic performance of the PV-fed grid-forming MLI.

The characteristics of the VSG, specifically the virtual inertia J and the damping coefficient D, are determined according to the system's dynamic response. These parameters affect the transient behavior of the inverter and must be carefully selected to achieve a suitable compromise between fast response and stable operation. A step change in the

reference active power is implemented, and the subsequent transient behavior is examined for various values of J and D. The impact of virtual inertia is initially analyzed in Figure 4a, where the damping coefficient is held constant at D = 10, but the inertia J is changed. As seen in this figure, increasing the inertia leads to a reduced dynamic response and a longer settling time.

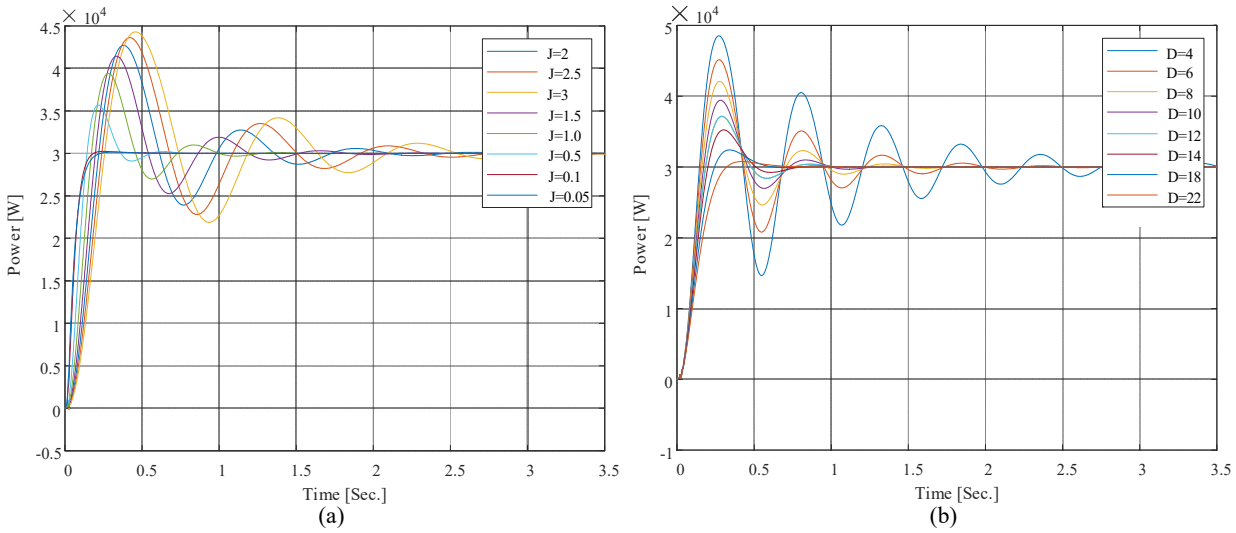


Figure 4. The active power response of the proposed VSG system under parameter variation: (**a**) the effect of virtual inertia J at fixed damping D = 10, and (**b**) the effect of damping coefficient D at fixed virtual inertia J = 1.0.

Furthermore, increased levels of J result in more significant oscillations in the active power response. Conversely, lower values of J yield a faster response with reduced oscillations. On the other hand, the influence of the damping coefficient is depicted in Figure 4b, where inertia remains constant, and D is changed. It is evident that increasing the damping coefficient substantially mitigates oscillations and enhances response stability. Reduced damping values produce prolonged oscillations and extended settling times.

Based on this analysis, to compromise between the fast response and the reduction in the oscillations, the parameters D = 10 and J = 0.05 are selected in this study.

The system and control parameters used in the simulations are summarized in Table 3. To assess the effectiveness of the proposed grid-forming system and the grid-forming control strategy, two representative simulation scenarios are considered.

Table 3. Parameters used in the simulation.

Parameter	Value
Nominal angular frequency (ω)	377 rad/s
Virtual inertia (J)	0.05
Damping coefficient (D)	10
Nominal voltage magnitude (U_s)	325 V
Inverter-side inductance (L_1)	3 mH
Grid-side inductance (L_3)	6 mH
Damping resistance (R_2)	0.5 Ω
Damping capacitance (C_2)	40 μF
Virtual resistance (R_1)	0.1 Ω
Grid-side resistance (R_3)	0.5 Ω

The first scenario examines the response of the PV-fed inverter under a step change in solar irradiance, while the second scenario investigates the system behavior under a step reduction in grid voltage, corresponding to a voltage sag condition, in order to examine the robustness of the proposed controller during external grid disturbances.

4.1. Case 1: Response Under Solar Irradiance Variation

In this scenario, the solar irradiance applied to the PV array is varied in order to evaluate the ability of the proposed grid-forming MLI to maintain stable operation under changes in renewable power generation. As shown in Figure 5, the irradiance is initially set to 500 W/m^2 and then increased to 1000 W/m^2 at $t = 1$ s. This step change represents a typical variation in solar conditions and allows for the dynamic interaction between the PV source, the DC-link voltage controllers, and the VSG-based grid-forming controller to be examined. As a result of this change, the maximum PV power extracted by the MPPT controller is shown in Figure 6. As seen in this figure, the MPPT technique operates correctly in extracting the available solar power of the PV panels.

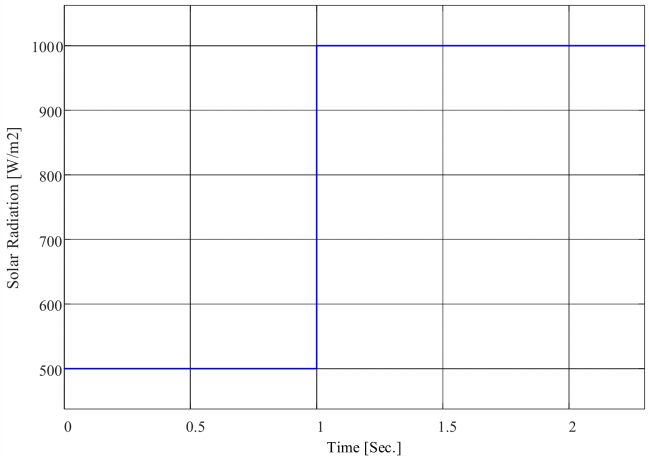


Figure 5. The solar irradiance profile applied to the PV array.

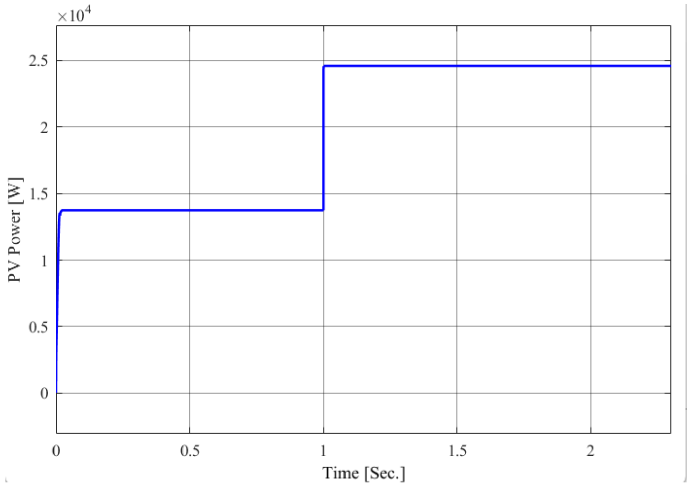


Figure 6. The maximum power extracted from the PV modules under irradiance variation.

The dynamic behavior of the six DC-link capacitors associated with the modified delta-connected CHB MLI is shown in Figure 7. It should be noted that only two cascaded H-bridge cells are utilized in the proposed MLI. The proposed DC-link supervisory controller accurately regulated the capacitor voltages around the reference voltage of approximately 300 V per cell. Moreover, after a step change in the solar radiation, the voltages converge

again to their steady-state values, demonstrating the effectiveness of the proposed DC-link control in maintaining voltage balance among the cascaded cells.

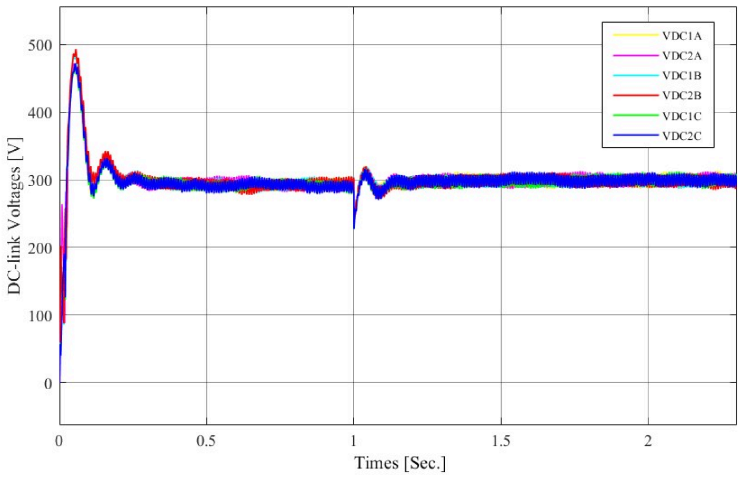


Figure 7. The DC-link voltages of the six cascaded H-bridge cells under irradiance variation.

From another point of view, the generated voltages from the proposed MLI are shown in Figure 8. Figure 8a shows the nine voltage levels of the line–line voltage (v_{AB}), while Figure 8b shows the generated voltage (v_{AZ}) across the transformer x and the generated voltage across the CHB of phase a (v_{ZB}). It should be noted that the voltage across each individual CHB arm or transformer generates a lower number of voltage levels (five voltage levels) compared to the overall line-to-line output voltage. This is because the modified delta-connected structure combines the voltages of multiple arms, as indicated in (1) and (2), where each line-to-line voltage is formed by the summation of two-phase voltages. Consequently, while each CHB arm produces a five-level voltage, their combination yields a greater number of levels in the line-to-line output, resulting in a nine-level waveform.

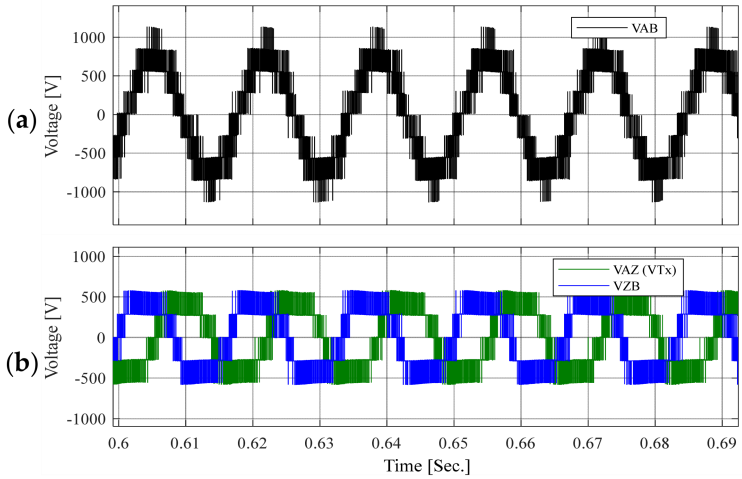


Figure 8. The generated voltages: (**a**) the nine-level line–line voltage, and (**b**) the voltage across the transformer x and the voltage across the CHB of phase a.

On the other hand, the behavior of the internal voltage references generated by the grid-forming controller is shown in Figure 9a,b, where the synchronous-frame voltage components V_d and V_q are compared with their respective references.

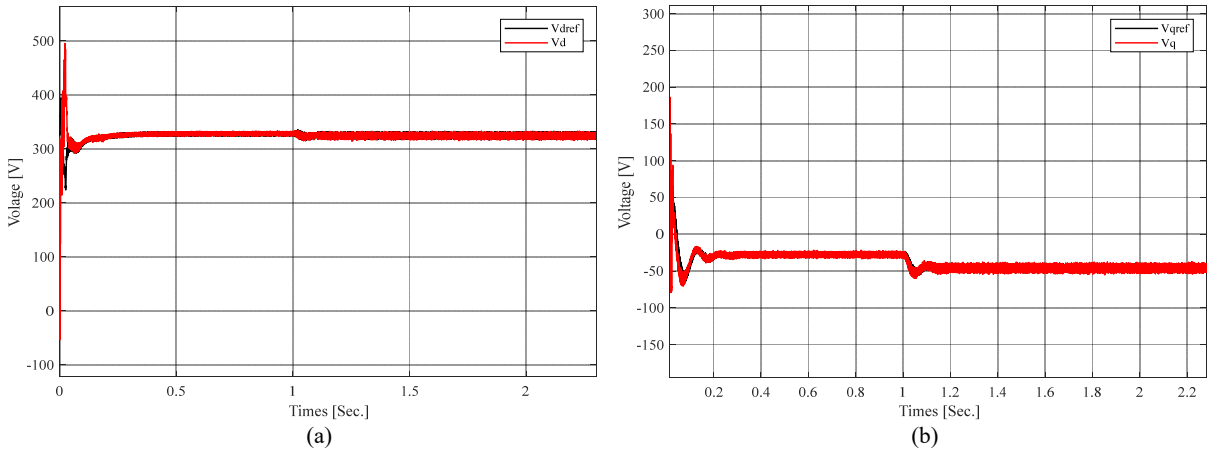


Figure 9. The reference generated internal voltages and the measured voltages: (**a**) d-axis, and (**b**) q-axis.

The corresponding frequency response of the VSG controller is depicted in Figure 10. The frequency initially deviates due to the sudden change in the available PV power and the resulting power imbalance at the PCC. However, the oscillations are rapidly attenuated by the damping term in the VSG swing equation, and the frequency returns to its nominal value of 60 Hz. This confirms that the selected inertia and damping parameters provide a stable and well-damped frequency response under irradiance variation.

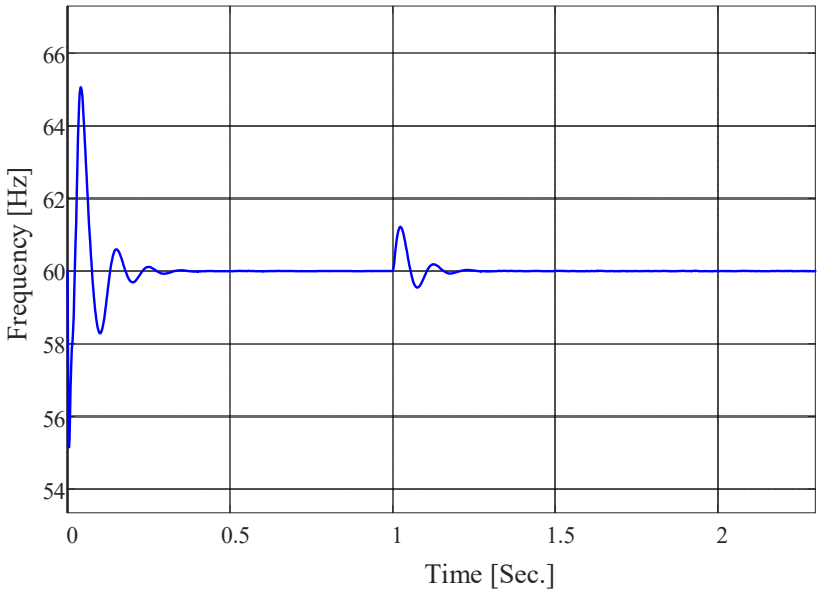


Figure 10. The frequency response of the VSG-controlled MLI.

The active power, reactive power, and power angle at the PCC are presented in Figure 11a–c. As shown in Figure 11a, the active power increases following the irradiance step since the MLI delivers the additional power generated by the PV modules to the grid. The transient response is well damped, and the system smoothly reaches a new steady-state operating point.

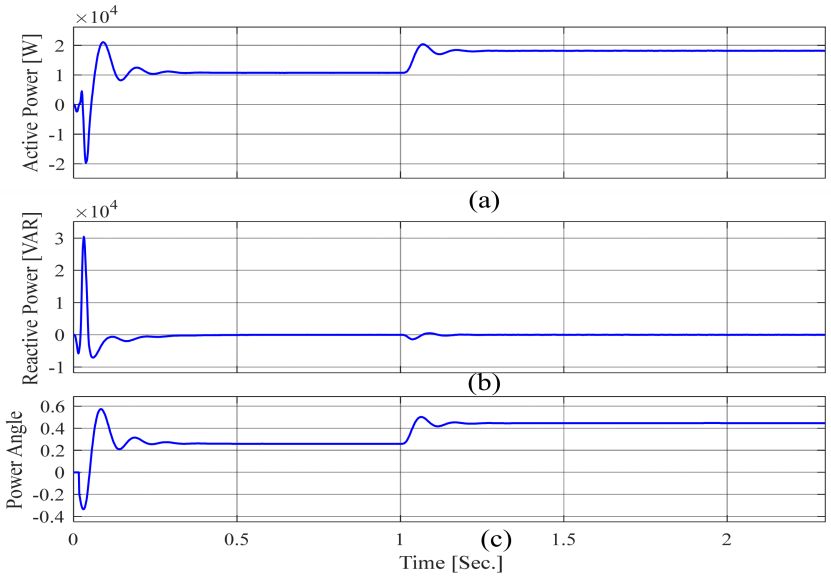


Figure 11. The power dynamics at the PCC under irradiance variation: (**a**) active power, (**b**) reactive power, and (**c**) the power angle.

In Figure 11b, the reactive power rapidly converges to the reference reactive power ($Q^* = 0$), which guarantees the MLI operates with a near-unity power factor under changing solar radiation conditions. The corresponding power angle evolution is shown in Figure 11c. The power angle was approximately 0.26 rad, and after the irradiance increase, the power angle shifted to approximately 0.45 rad in order to accommodate the increased active power transfer. This behavior is consistent with the classical synchronous-machine power transfer relationship, where the transmitted active power is proportional to the sine of the power angle.

The transient oscillations observed immediately after the disturbance are effectively attenuated due to the damping term in the VSG swing equation. The selected damping coefficient, therefore, provides sufficient suppression of electromechanical oscillations and ensures stable synchronization of the GFI.

The following results further examine the dynamic behavior predicted by the reduced-order small-signal model presented in Section 3, particularly the influence of damping variation on the coordinated interaction between the DC-link dynamics and the frequency response. Figure 12a–c show a comparison obtained by reducing the damping coefficient from $D = 10$ to $D = 4$, while maintaining the virtual inertia fixed at $J = 0.05$. The figure shows the system dynamic response, including (a) frequency variation, (b) fluctuations in the DC-link voltages, and (c) power dynamics. Figure 12a reveals that decreasing the damping coefficient from $D = 10$ to $D = 4$ leads to increased oscillations and slower decay in the frequency response. This behavior aligns with VSG dynamics, wherein the damping coefficient directly influences the attenuation of oscillations. The DC-link voltages in Figure 12b also exhibit larger oscillations under low damping conditions, indicating a stronger interaction between the DC-side energy and the AC-side dynamics. Similarly, the power responses in Figure 12c show increased fluctuations, confirming that insufficient damping affects the overall system stability. These results highlight the importance of proper damping selection to ensure stable and well-damped grid-forming operation.

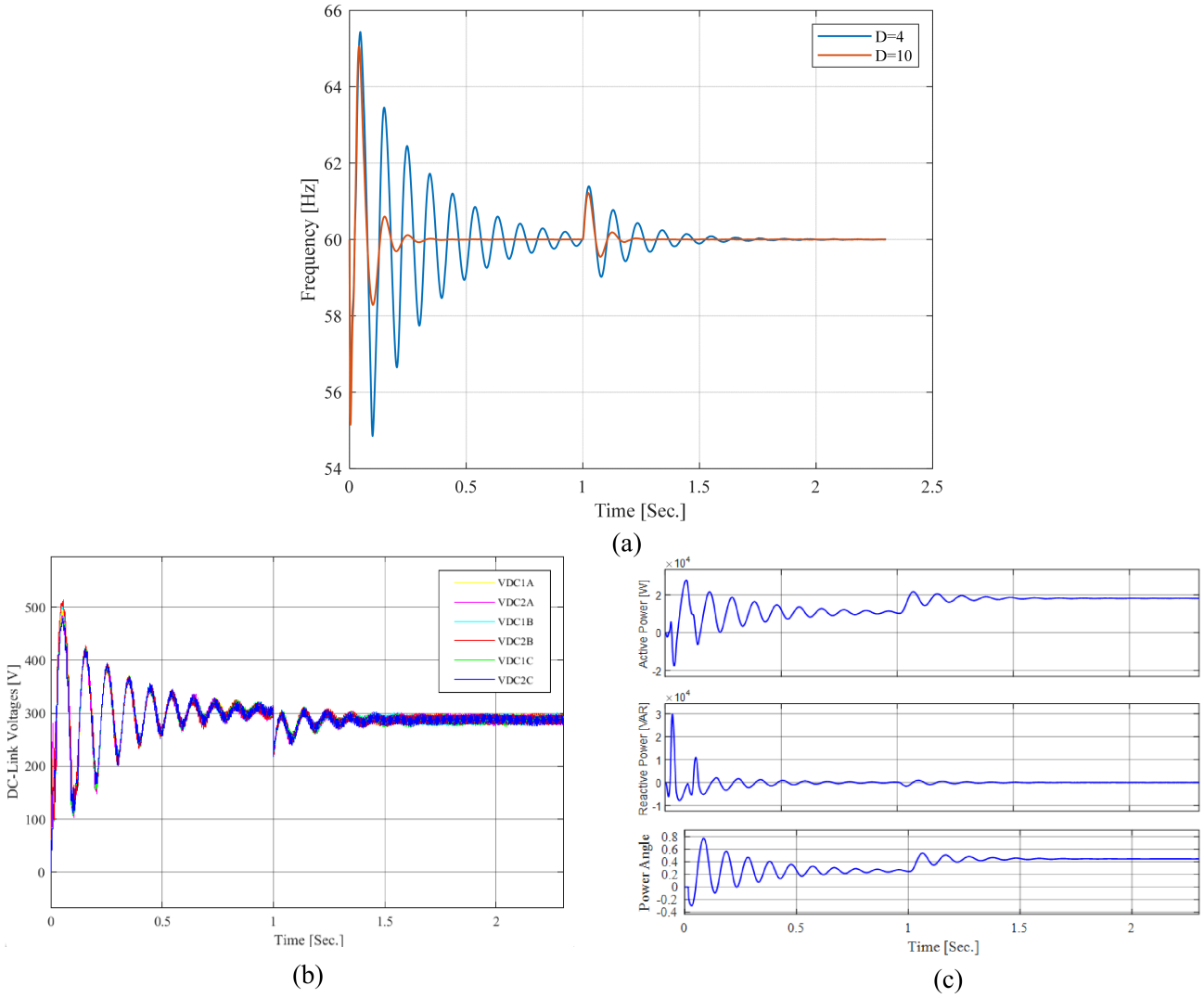


Figure 12. The dynamic response of the proposed VSG system under parameter variation (D = 4, J = 0.05): (**a**) the frequency response, (**b**) DC-link voltages, and (**c**) active and reactive power dynamics.

Moreover, the three-phase grid voltages, PCC voltages, and injected grid currents change during irradiance, corresponding to the selected operating parameters ($D = 10, J = 0.05$). Figure 13a presents the grid voltages V_{gA}, V_{gB}, and V_{gC}, which remain balanced and sinusoidal. Figure 13b shows the PCC voltages V_{pccA}, V_{pccB}, and V_{pccC}.

It can be observed that the PCC voltages closely follow the grid voltages and are a little higher than the grid voltages, allowing the power to be injected to the grid side, indicating proper synchronization and the stable voltage-forming operation of the inverter. Figure 13c illustrates the grid currents I_{gA}, I_{gB}, and I_{gC} before and after the step change in the solar radiation. Note that the currents are in phase with the grid voltages, confirming that the MLI operates with a near-unity power factor. Moreover, the harmonic spectrum of the grid current i_A is shown in Figure 14. As shown in this figure, the THD of the grid current is 0.5%, which is well below the limits specified by IEEE 519 standards.

The simulation results provided in this case demonstrate that the modified delta-connected CHB MLI combined with the VSG-based control and DC-link supervisory regulation is capable of maintaining stable grid-forming operation while accommodating variations in renewable power generation.

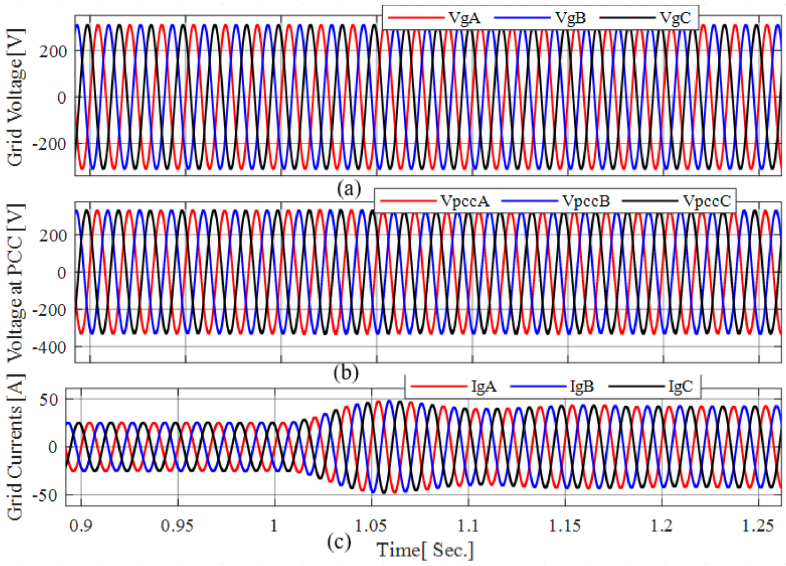


Figure 13. Three-phase grid interaction during irradiance variation: (**a**) grid voltages, (**b**) PCC voltages, and (**c**) injected grid currents.

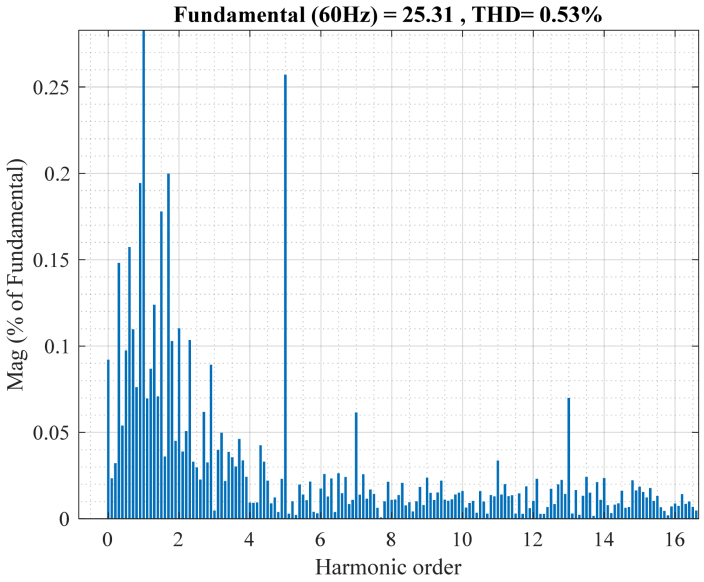


Figure 14. The harmonic spectrum of the grid current i_A.

4.2. Case 2: System Response Under Grid Voltage Sag

To further evaluate the robustness of the proposed GFI, a second scenario is considered, in which the system is subjected to a grid voltage disturbance. In this case, the solar irradiance is kept constant so that the PV power generation remains unchanged during the test. This allows the dynamic response of the inverter and the associated control strategy to be analyzed under grid-side disturbances.

A temporary voltage sag is introduced in the grid voltage between 0.5 s and 0.8 s, during which the RMS voltage decreases from its nominal value of 380 V to approximately 300 V (≈0.79 pu) (Figure 15). After the disturbance period, the grid voltage returns to its nominal level. This test is intended to evaluate the ability of the proposed VSG-based control and DC-link supervisory regulation to maintain stable operation during grid voltage variations.

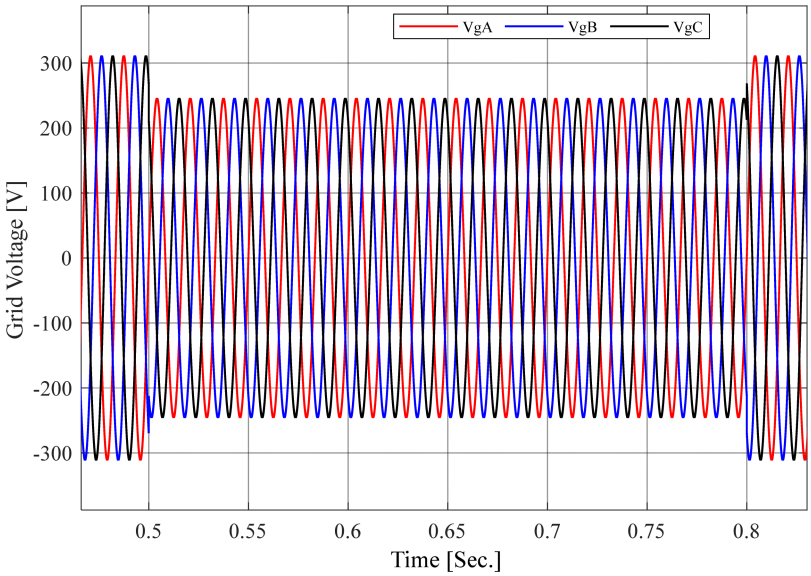


Figure 15. The voltage disturbance for the three-phase grid voltages.

The response of the DC-link voltages in the proposed system is shown in Figure 16. Notwithstanding the grid disturbance, the DC-link voltages are effectively maintained near their reference values, exhibiting only minor transient fluctuations. This behavior illustrates the efficacy of the proposed DC-link supervisory control strategy in sustaining a stable energy equilibrium within the modified delta-connected CHB MLI, while the controller guarantees that the DC-side voltages remain regulated evenly during grid disturbances, which is essential for the reliable operation of PV-based grid-forming MLI.

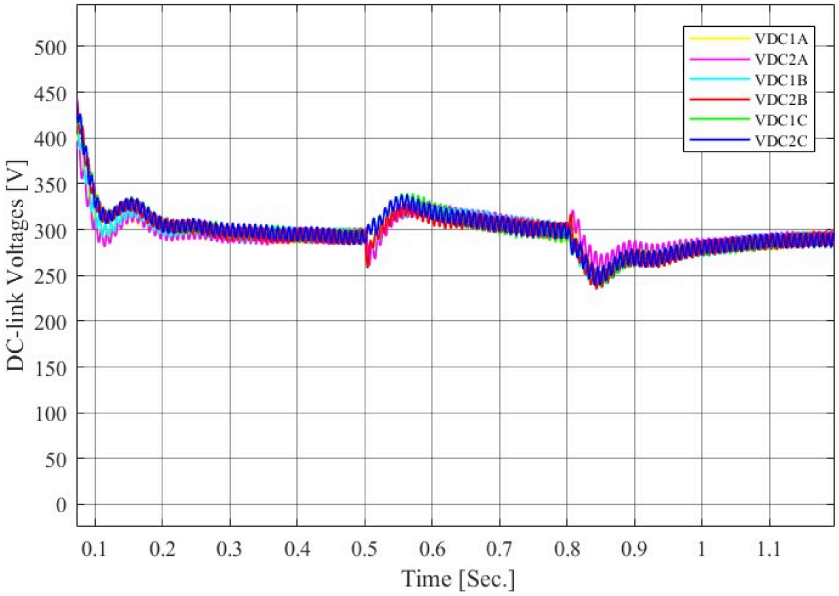


Figure 16. The DC-link voltages of the cascaded H-bridge cells during the voltage sag disturbance.

The corresponding frequency response of the VSG controller is depicted in Figure 17. At the instant of the disturbance, a small frequency deviation occurs as the swing equation reacts to the temporary imbalance between the internal synchronization power and the measured active power at the PCC. The damping term included in the proposed VSG control effectively attenuates the oscillations, allowing the frequency to quickly return to its nominal value of 60 Hz. This behavior demonstrates the stabilizing role of the damping coefficient in suppressing electromechanical oscillations during grid disturbances. The

limited frequency deviation and smooth recovery indicate that the selected inertia and damping values ensure stable operation and maintain synchronization under voltage sag conditions.

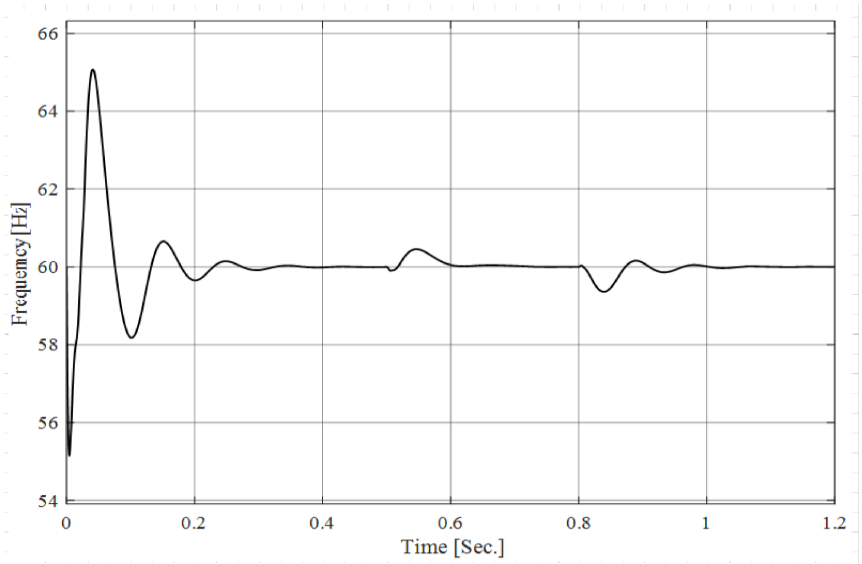


Figure 17. The frequency response of the VSG-controlled inverter during the voltage sag.

On the other hand, the power response of the system is presented in Figure 18, which shows the active power, reactive power, and power angle at the PCC. Since the PV generation remains constant, the active power delivered to the grid is largely maintained during the grid voltage disturbance, as shown in Figure 18a. Moreover, the proposed control scheme maintains the reactive power at zero value to guarantee a unity power factor, as seen in Figure 18b. The variation in the power angle shown in Figure 18c reflects the transient dynamics of the VSG control and the adjustment of the inverter's internal voltage angle to maintain synchronization with the grid.

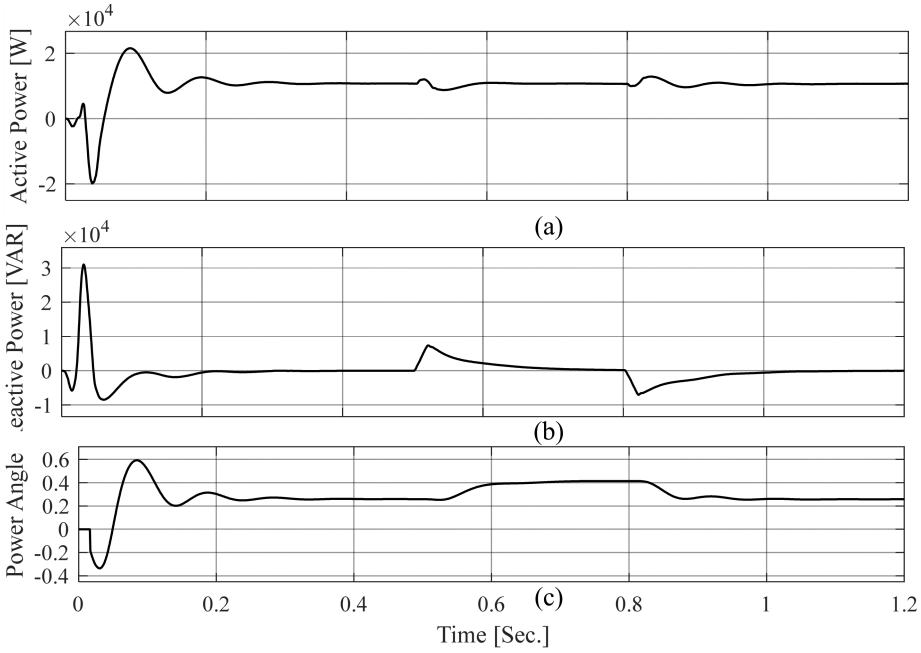


Figure 18. The power dynamics at the PCC during the voltage sag: (**a**) active power, (**b**) reactive power, and (**c**) the power angle.

Finally, Figure 19 illustrates the PCC voltages and the injected grid currents. During the sag interval, the PCC voltage magnitude decreases following the grid voltage reduction. The MLI compensates for the voltage drop by increasing the current magnitude in order to sustain power transfer. The currents remain balanced and sinusoidal throughout the disturbance, indicating that the proposed control strategy preserves power quality even under abnormal grid conditions.

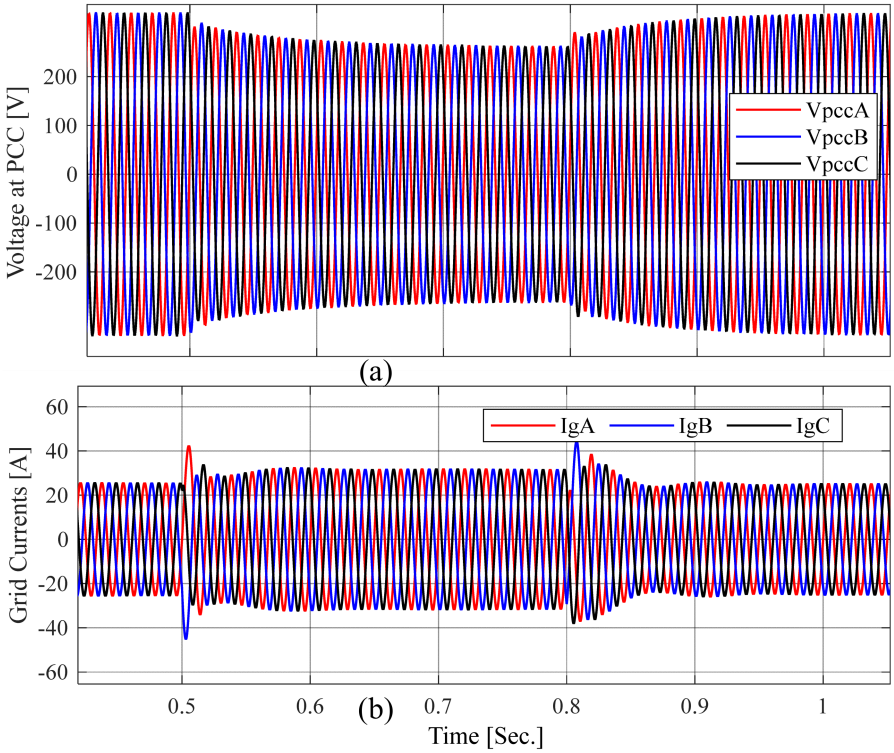


Figure 19. The grid-side electrical variables during the voltage sag: (**a**) the PCC voltages, and (**b**) the injected grid currents.

Overall, the results confirm the applicability of the modified delta-connected CHB topology in grid-forming PV systems and demonstrate its stable performance under different operating conditions.

5. Conclusions

This paper introduces a VSG based on a multilevel inverter using isolated Cúk converters for MPPT operation for PV-grid interconnection that is capable of ensuring stable voltage and frequency support. The proposed VSG system is based on a modified delta-connected CHB MLI that generates the same voltage levels as the star-connected CHB MLI using a lower number of components compared to the conventional delta-connected CHB MLI. Moreover, the proposed topology enhances voltage quality and current waveform, reduces voltage stress on switches, and is modular with inherent voltage balancing capability, making it suitable for VSG operation. A comprehensive mathematical model of the VSG is investigated to represent the dynamics of the swing equation, DC-link voltages, MLI, filter, and control loops. The selection of VSG parameters is also investigated, highlighting the importance of coordinated tuning of inertia and damping to achieve a desirable trade-off between dynamic response and stability. The simulation model is tested under variations in solar radiation and grid-voltage disturbances to evaluate the performance of the proposed topology and control scheme. The results show that the proposed system maintains stable DC-link voltages, regulates the frequency effectively, and provides stable power injection

with well-damped transient behavior. In addition, the effect of VSG parameter variation is also examined. It can be observed that changing the damping coefficient has a clear impact on the frequency response, DC-link voltages, and overall system behavior, highlighting the importance of proper parameter selection. Overall, the proposed system represents a promising and competitive solution that combines a multilevel topology with inherent structural advantages and a grid-forming control strategy for PV-based applications under the considered operating conditions.

Funding: This work was funded by Prince Sattam bin Abdulaziz University, project number (PSAU/2025/01/33400).

Data Availability Statement: The original contributions presented in this study are included in the article. Further inquiries can be directed to the corresponding author.

Acknowledgments: The authors extend their appreciation to Prince Sattam bin Abdulaziz University for funding this research work through the project number (PSAU/2025/01/33400).

Conflicts of Interest: The authors declare no conflict of interest.

References

1. Abudyak, Y.H. Grid-Forming Inverters: Comprehensive Review, Design, and Implementation of Advanced Control Methods. Master's Thesis, University of Central Florida, Orlando, FL, USA, 2025.
2. Mohammed, N.; Udawatte, H.; Zhou, W.; Hill, D.J.; Bahrani, B. Grid-forming inverters: A comparative study of different control strategies in frequency and time domains. *IEEE Open J. Ind. Electron. Soc.* **2024**, *5*, 185–214. [CrossRef]
3. Awda, Y.; Alowaifeer, M. Adaptive optimization of virtual synchronous generator based on fuzzy logic control and differential evolution. *Ain Shams Eng. J.* **2024**, *15*, 102606. [CrossRef]
4. Zhong, Q.-C.; Weiss, G. Synchronverters: Inverters that mimic synchronous generators. *IEEE Trans. Ind. Electron.* **2011**, *58*, 1259–1267. [CrossRef]
5. Driesen, J.; Visscher, K. Virtual synchronous generators. In Proceedings of the IEEE Power & Energy Society General Meeting, Pittsburgh, PA, USA, 20–24 July 2008.
6. Memon, A.J.; Mahar, M.A.; Larik, A.S.; Shaikh, M.M. A comprehensive review of reduced device count multilevel inverters for pv systems. *Energies* **2023**, *16*, 5638. [CrossRef]
7. Zhang, X.; Hu, Y.; Mao, W.; Zhao, T.; Wang, M.; Liu, F.; Cao, R. A grid-supporting strategy for cascaded H-bridge PV converter using VSG algorithm with modular active power reserve. *IEEE Trans. Ind. Electron.* **2020**, *68*, 186–197. [CrossRef]
8. Wang, R.; Wang, Y.; Zhang, P.; Sun, Q.; Gui, Y.; Wang, P. System modeling and robust stability region analysis for multi-inverters based on VSG. *IEEE J. Emerg. Sel. Top. Power Electron.* **2024**, *12*, 6042–6052. [CrossRef]
9. Mateus, T.H.d.A.; Pomilio, J.A.; Godoy, R.B.; Pinto, J.O.P. VSG Control Applied to Seven-Level PV Inverter for Partial Shading Impact Abatement. *Energies* **2022**, *15*, 6409. [CrossRef]
10. Balal, A.; Dinkhah, S.; Shahabi, F.; Herrera, M.; Chuang, Y.L. A review on multilevel inverter topologies. *Emerg. Sci. J.* **2022**, *6*, 185–200. [CrossRef]
11. Noman, A.M.; Al-Shamma'a, A.A.; Asef, P.; Alkuhayli, A. Hybrid cascaded MLI development for PV-grid connection applications. *IET Power Electron.* **2023**, *16*, 1717–1731. [CrossRef]
12. Mosepele, B.; Samikannu, R.; Amuhaya, L. A structural review on reduced switch count and hybrid multilevel inverters. *Front. Energy Res.* **2024**, *12*, 1396149. [CrossRef]
13. He, Z.; Ma, F.; Xu, Q.; Chen, Y.; Li, C.; Li, M.; Guerrero, J.M.; Luo, A. Reactive power strategy of cascaded delta-connected STATCOM under asymmetrical voltage conditions. *IEEE J. Emerg. Sel. Top. Power Electron.* **2017**, *5*, 784–795. [CrossRef]
14. Ray, I.; Tolbert, L.M. Grid-forming inverter control design for PV sources considering DC-link dynamics. *IET Renew. Power Gener.* **2025**, *19*, e12454. [CrossRef]
15. Mallik, R.; Majmunovic, B.; Dutta, S.; Seo, G.-S.; Maksimovic, D.; Johnson, B. Control design of series-connected PV-powered grid-forming converters via singular perturbation. *IEEE Trans. Power Electron.* **2023**, *38*, 5091–5106. [CrossRef]
16. Hossein Nataj, S.; Gholamian, S.A.; Rezanejad, M.; Mehrasa, M. Virtual synchronous generator-based control of modular multilevel converter for integration into weak grid. *IET Renew. Power Gener.* **2023**, *17*, 3097–3107. [CrossRef]
17. Poulose, A.; Kim, S. Transient stability analysis and enhancement techniques of renewable-rich power grids. *Energies* **2023**, *16*, 2495. [CrossRef]
18. Shintai, T.; Miura, Y.; Ise, T. Oscillation damping of a distributed generator using a virtual synchronous generator. *IEEE Trans. Power Deliv.* **2014**, *29*, 668–676. [CrossRef]

19. Hosny, M.; Marei, M.I.; Mohamad, A.M. Adaptive hybrid virtual inertia controller for PMSG-based wind turbine based on fuzzy logic control. *Sci. Rep.* **2024**, *15*, 3757. [CrossRef]
20. Yang, X.; Li, H.; Jia, W.; Liu, Z.; Pan, Y.; Qian, F. Adaptive virtual synchronous generator based on model predictive control with improved frequency stability. *Energies* **2022**, *15*, 8385. [CrossRef]
21. Khamisov, O.O.; Vasilev, S.P. Dynamic virtual inertia and damping control for zero-inertia grids. *arXiv* **2024**, arXiv:2411.03998. [CrossRef]
22. Rajak, M.K.; Pudur, R. Multiobjective adaptive predictive virtual synchronous generator control strategy for grid stability and renewable integration. *Sci. Rep.* **2025**, *15*, 9241. [CrossRef]
23. Chen, Y.; Han, W.; Hu, Y.; Zhang, Y. Adaptive control for improved virtual synchronous generator under imbalanced grid voltage. *IEEE Open J. Ind. Electron. Soc.* **2024**, *5*, 722–737. [CrossRef]
24. Li, K. Adaptive virtual synchronous generator control strategy based on coordinated parameter adjustment. *Electronics* **2024**, *13*, 4318.
25. Du, M.; Mei, H. The application of virtual synchronous generator technology in inertial control of new energy vehicle power generation. *Front. Mech. Eng.* **2024**, *10*, 1382664.
26. Nourelhouda, D.; Daili, Y.; Harrag, A. A review of recent control techniques of virtual synchronous machine for renewable energy. *Sci. Bull. Electr. Eng. Fac.* **2024**, *23*, 20–32.
27. Albornoz, M.; Rohten, J.; Espinoza, J.; Varela, J.; Sbarbaro, D.; Gallego, Y. Photovoltaic power injection control based on a virtual synchronous machine strategy. *Sensors* **2024**, *24*, 4039. [CrossRef] [PubMed]
28. Zheng, Y.; Xu, Y.; Yang, Y.; Hua, L.; Yang, Y. Application of adaptive virtual synchronous generator based on improved active power loop in photovoltaic storage systems. *Front. Energy Res.* **2025**, *12*, 1468629. [CrossRef]
29. Rizi, H.S.; Chen, Z.; Huang, A.Q.; Rodriguez, P. A comprehensive strategy for grid-forming control in DC-coupled photovoltaic and battery energy storage inverters. In Proceedings of the IEEE 15th International Symposium on Power Electronics for Distributed Generation Systems (PEDG), Luxembourg, 23–26 June 2024.
30. Noman, A.M. A Novel Modified Delta-Connected CHB Multilevel Inverter with Improved Line–Line Voltage Levels. *Electronics* **2025**, *14*, 1711. [CrossRef]

Disclaimer/Publisher's Note: The statements, opinions and data contained in all publications are solely those of the individual author(s) and contributor(s) and not of MDPI and/or the editor(s). MDPI and/or the editor(s) disclaim responsibility for any injury to people or property resulting from any ideas, methods, instructions or products referred to in the content.